Limitations in one-dimensional (an)elastic Earth models for explaining GPS-observed M$_2$ Ocean Tide Loading displacements in New Zealand

Bogdan Matviichuk[1,1], Matt A King[1,1], Christopher Stephen Watson[1,1], and Machiel Simon Bos[2,2]

[1]University of Tasmania
[2]University of Beira Interior, Institute D. Luis

November 30, 2022

Abstract

GPS observations of ocean tide loading displacements can help infer the regional anelastic properties of the asthenosphere. We estimate M2 ocean tide loading displacements at 170 GPS sites in New Zealand and compare these to modeled values using a range of numerical tide and radially symmetric (1D) elastic and anelastic Earth models. Regardless of the model combination we are unable to reduce the strong spatial coherence of the M2 residuals across the North Island where they reach 0.4 mm (2%). The best fit in the North Island is obtained when combining the FES2014b tide model with spatially-variable ocean density and water compressibility, and the STW105 Earth model. The residuals exhibit a change of ˜0.3 mm in magnitude between the Taupo Volcanic Zone and the east coast (˜100 km), suggesting that this region's laterally-varying, shallow rheological structure may need to be considered to explain these observations.

Limitations in one-dimensional (an)elastic Earth models for explaining GPS-observed M_2 Ocean Tide Loading displacements in New Zealand

Bogdan Matviichuk[1], Matt A. King[1], Christopher S. Watson[1] and Machiel S. Bos[2*]

[1]School of Geography, Planning, and Spatial Sciences, University of Tasmania, Hobart, 7001, Australia
[2]Instituto Dom Luiz (IDL), University of Beira Interior, Covilhã, Portugal

Key Points:

- M_2 ocean tide loading displacements in New Zealand are inferred from GPS observations
- Estimates for the North Island are not reproduced by models combining ocean tide loading and a 1D (an)elastic Earth structure
- Spatially-coherent residual displacements of ∼0.4 mm (2%) are likely due to lateral Earth structure associated with Pacific Plate subduction

*supported by the project FCT/UIDB/50019/2020 – IDL funded by FCT

Corresponding author: B. Matviichuk, `bogdan.matviichuk@utas.edu.au`

Abstract

[GPS observations of ocean tide loading displacements can help infer the regional anelastic properties of the asthenosphere. We estimate M_2 ocean tide loading displacements at 170 GPS sites in New Zealand and compare these to modeled values using a range of numerical tide and radially symmetric (1D) elastic and anelastic Earth models. Regardless of the model combination we are unable to reduce the strong spatial coherence of the M_2 residuals across the North Island where they reach 0.4 mm (2%). The best fit in the North Island is obtained when combining the FES2014b tide model with spatially-variable ocean density and water compressibility, and the STW105 Earth model. The residuals exhibit a change of ∼0.3 mm in magnitude between the Taupo Volcanic Zone and the east coast (∼100 km), suggesting that this region's laterally-varying, shallow rheological structure may need to be considered to explain these observations.]

Plain Language Summary

[The solid Earth changes shape due to the changing weight of the ocean as the ocean tides rise and fall. Measuring this change and comparing it to predictions can yield insights into the interior properties of the Earth, tens to hundreds of kilometers below the surface. We used GPS to measure the changing shape of New Zealand and compared it to predictions based on a range of Earth and tide models. The difference between the observed and modeled displacements revealed a complicated pattern over New Zealand, especially in the North Island and specifically near the Taupo Volcanic Zone. Due to the high accuracy of our GPS analysis and the ocean tide models, the observed residuals provide information about the elastic properties of the Earth and the complex geological structure of the region. The observed significant misfits show limitations of the 1D Earth model that varies only with depth which is standard in geodetic analysis.]

1 Introduction

The asthenosphere, the weak viscoelastic substrate beneath the lithosphere, is fundamental to the concept of plate tectonics and the earthquake cycle (Hu et al., 2016). The rheological properties of the asthenosphere are, however, not well understood (Karato, 2012). The importance of the asthenosphere is amplified at active convergent boundaries of tectonic plates, specifically subduction systems that initiate forces principal in driving plate tectonics and mantle convection (Stern, 2004). New Zealand is split by the transform Alpine Fault and is locked between two subduction systems: the Hikurangi in the north and Puysegur in the south (Lamarche & Lebrun, 2000). These lithospheric discontinuities should produce the large perturbations observable in the earth tide and perhaps the ocean load tide displacements (Zürn et al., 1976).

Analysis of Ocean Tide Loading, a phenomenon created by the solid Earth's response to tidal-water mass redistribution, can be used to validate ocean tide models and elastic Earth models at tidal periods (e.g., Farrell, 1972b; Martens et al., 2016; Yuan et al., 2013; Yuan & Chao, 2012). More recently GPS-derived Ocean Tide Loading Displacements (OTLD) have been used to constrain the asthenosphere's anelasticity at the period of the major M_2 tidal constituent (period of 12.42 h) by showing improved agreement with deformation modeled using anelastic Earth models. To date, studies of asthenosphere anelasticity have focused on continental settings such as western Europe, western USA, South America, the eastern China Sea region and Alaska (Bos et al., 2015; Ito & Simons, 2011; Martens & Simons, 2020; Wang et al., 2020).

In this paper, we examine the tidal deformation of New Zealand, at the dominant M_2 tidal period, using an array of continuous GPS stations. We combine recent ocean tide models with a range of purely elastic and anelastic 1D Earth models and compare modeled deformation with GPS observed estimates to further understand the anelastic properties of the asthenosphere beneath New Zealand.

2 Methods

2.1 GPS Data and Analysis

We analyzed all available continuously operating GNSS stations in New Zealand over the period from the beginning of 2013 to mid-2020 (doy 153), chosen to maximize the number of stations with overlapping data and minimize data gaps in individual stations. Over this seven-year period, data are available from 170 stations, with all but two (CHTI and RAUL) located on mainland New Zealand (see Table S1 for a full list of sites). These stations were designed for nationwide coverage with station spacing in the range 80–100 km to monitor and control the national datum and for geophysical studies (Gale et al., 2015). As shown in Fig. 1, the network provides approximately uniform (but sparse) coverage in the South Island with a substantially higher spatial density of coverage across much of the North Island.

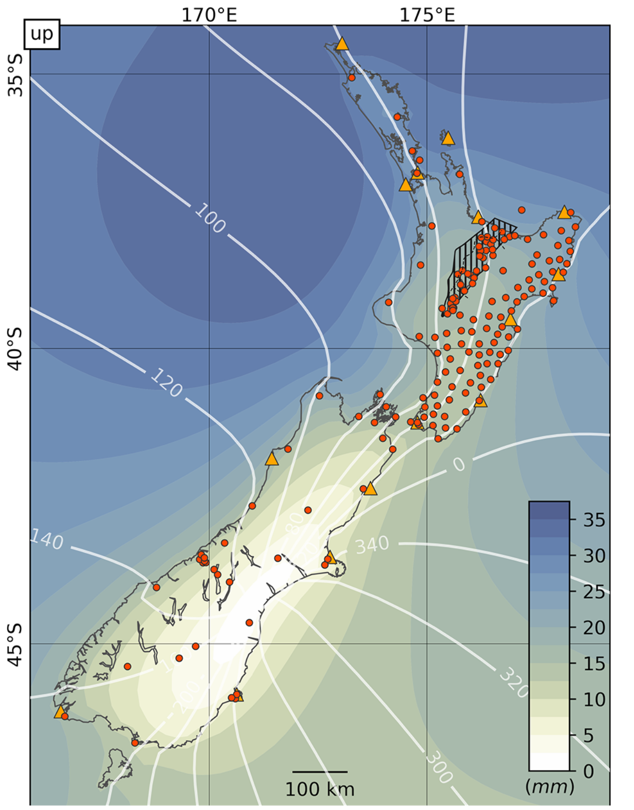

Figure 1. Map of New Zealand showing modeled M_2 Up OTLD amplitude and phase (relative to Greenwich) computed with TPXO7.2 ocean tide model and PREM Green's function. GPS sites and tide gauge locations are represented by red circles and orange triangles, respectively. The hatched area in the North Island represents the approximate region of the Taupo Volcanic Zone.

These data were analyzed using GipsyX v1.3 software (Bertiger et al., 2020) using a kinematic Precise Point Positioning (PPP) approach (Zumberge et al., 1997). The dataset processing was fascilitated by a custom wrapper (Matviichuk, 2020). Our approach was described in full by Matviichuk et al. (2020) with the main difference being that here we used only the GPS data. Data from other GNSS (e.g. GLONASS) were not logged at all sites over this period hence was excluded from this analysis. We used NASA JPL's orbit and clock products from their third internal reprocessing campaign (repro

3.0, released March 2018). Ambiguities were fixed to integers where possible (Bertiger et al., 2010). Earth body tides were modeled within GipsyX according to IERS 2010 Conventions (Petit & Luzum, 2010).A priori OTLD values were removed based on the FES2004 ocean tide model (Lyard et al., 2006) and Gutenberg-Bullen purely-elastic Earth model (Farrell, 1972a) in a centre-of-mass of the whole Earth system frame (`holt.oso.chalmers.se/loading`) – we later restored the OTLD component at the coordinate time series level for further study; this remove-restore approach is done to reduce the magnitude of companion tides and follows approaches adopted previously (e.g., Abbaszadeh et al., 2020; Matviichuk et al., 2020; Penna et al., 2015).

The GipsyX coordinate and zenith-wet-delay process noise values were chosen based on the tests of Penna et al. (2015), Wang et al. (2020) and Matviichuk et al. (2020), using values of 3.2 mm/sqrt(s) and 0.1 mm/sqrt(s), respectively. Our parameterization produces coordinate estimates every 300 s from which we remove large outliers identified with clock bias estimates larger than 3×10^3 meters and residuals to a detrended timeseries that are larger than $\pm3\sigma$ of each global cartesian coordinate component. These timeseries were converted to local topocentric east, north and up components which were then further analyzed.

2.2 OTLD Models

We focus here on the difference between the GPS-derived OTLD and those modeled based on ocean tide models and elastic and anelastic Earth models. For the tides we mainly consider three relatively recent global ocean tide models: GOT4.10c (Ray, 2013), TPXO9.v1 (Egbert & Erofeeva, 2002) and FES2014b (Carrere et al., 2016), although we also explore FES2012 (Carrere et al., 2013) and FES2004 (Lyard et al., 2006). We also consider one regional New Zealand tide model (Walters et al., 2001), EEZ, which we combine with FES2014b outside the model's domain for loading computations. We used bicubic interpolation to resample the models to a common $0.05\times0.05°$ grid. We note that the TPXO9.v2a model was also later analyzed but we found no improvement relative to TPXO9.v1 model present in the analysis.

The amplitude of the M_2 tide reaches over 1 m near the coast of New Zealand, due to the shallow bathymetry, and decreases to 10-20 cm in the open ocean (Stammer et al., 2014). The pattern of M_2 between the two islands of New Zealand is similar to an amphidromic point although the amplitudes are not zero. As a result, the tides to the east and west of New Zealand are out of phase and partly cancel out each other's contribution to the total OTLD value in the up component.

All modeled OTLD values were computed using the CARGA software (Bos & Baker, 2005). The coastline was taken from the GMT database (Wessel & Smith, 1996) and has a resolution of around 150 m. In most studies a constant sea water density is assumed, for example 1030 kg/m^3. Ray (2013) advocated to take the spatial variation of the density into account, and even the fact that water is slightly compressible, which means that the mean density of a water column should increase due to the extra density at the bottom of the column. For the ocean around New Zealand the effect on the resultant deformation is around 1-3%. Assuming a mean 2% effect and a mean OTLD amplitude of 20 mm, this corresponds to a potential error of 0.4 mm which is too large to be ignored. We have implemented the equations of Ray (2013) and obtained mean density values from the World Ocean Atlas 2013 - WOA13 (Zweng et al., 2013)based on a $0.25\times0.25°$ grid.

Three Green's functions were assessed with this set of ocean tide models: PREM (Dziewonski & Anderson, 1981), STW105 (Kustowski et al., 2008) and S362ANI (Kustowski et al., 2008). PREM and STW105 provide radial (1D) profiles for the density, and seismic velocities Vp and Vs. These profiles were used to compute load Love numbers which were converted into Green's functions (Bos & Scherneck, 2013). The method is based on Alterman et al. (1959) but uses the more recent Chebyshev collocation method to solve the differential equations (Guo et al., 2001). These profiles are based on seismic data and are only valid at a period of 1 s. To convert them to the period of the M_2 constituent, a constant absorption band (Q=constant, see Table S5) is assumed between these two periods (Bos et al., 2015). S362ANI is based on STW105 but has a shear velocity that varies horizontally, not just by depth. Given our focus on 1D radially symmetric models, we averaged the values in a rectangular region between 48°S and 33°S and 165°E and 180°E to yield a model representative of the average values over the study region. Once converted into a radially symmetric model, the Green's function for S362ANI was computed in similar manner as PREM and STW105.

2.3 OTLD Analysis

Amplitudes and phases of tidal constituents, and their uncertainties, were estimated from the GPS coordinate timeseries using the Eterna software v.3.30 (Wenzel, 1996) for 17 tidal constituents, with local phases converted to Greenwich phases with lags positive to enable comparison with the models of OTLD. Our focus is solely on the largest loading constituent in New Zealand, M_2, the major semi-diurnal lunar constituent. To decrease the computation time and measurement noise, the timeseries were first downsampled to 30-min through window averaging.

Before computing the residuals, we assessed the impact from the differences in the ocean tide models on the modeled OTLD values. For this we computed errors associated with differences between the three global ocean tide models: FES2014b, GOT4.10c and TPXO9.v1 (Fig. S3). The errors are consistent over most sites with a mean error value of ∼0.1 mm in all three components. We follow the naming conventions of Yuan and Chao (2012) with observed and modeled OTLD referred to as Z_{obs} and Z_{OTL} respectively with Z_{res} being their vector difference. We refer to the magnitude of the vector difference as $\|Z_{res}\|$.

3 Results

3.1 Preliminary analysis of the ocean tide models

We expected local EEZ ocean tide model to perform similarly to the most recent global tide models at the M_2 period. We computed an average of the three most recent ocean tide models: FES2014b, GOT4.10c, and TPXO9.v1 (Fig. 2a) to provide a baseline for the assessment of the EEZ model. We added the FES2004 global model to the comparison to assess the performance of global model recommended within the IERS 2010 Conventions for geodetic analysis (Petit & Luzum, 2010). Compared with the newer global models, FES2004 demonstrated higher discrepancies (up to 1 m) in the semi-closed water bodies and shallow bights (Fig. S1a), while the EEZ regional tide model shows an approximately constant vector difference in the shallow sea waters (<1000 m depth) of around 0.1 m (Fig. S1b).

We assess the tide models further by comparing modeled M_2 tide values with those from 15 tide gauges, shown in Fig. 1. The mean of the M_2 amplitude differences are shown in Table 1 demonstrating that the EEZ model exhibits over 5-7 cm amplitude difference relative to tide gauges. The other global models have mean amplitude differences of 1.13-3.05 cm, with the GOT4.10c model in closest agreement in terms of mean amplitude difference at the tide gauges (see Table S5 for details).

To assess the variation between recent global ocean tide models at the M_2 period we computed the inter-model standard deviation (Fig. 2b). We found M_2 standard deviation (SD) values of 0.18 cm and 2.68 cm for the deep ocean (>1000 m depth) and the shallow sea (<1000 m depth) respectively. These values are smaller by 40% and 20% than globally derived values reported by Stammer et al. (2014) for M_2. The largest SD values of up to 0.6 m are located in the Hauraki Gulf in the western North Island, which indicates the region where the largest ocean tides errors are expected. We note however that this is a very small region and hence will likely have negligible impact on most modeled displacements considered here.

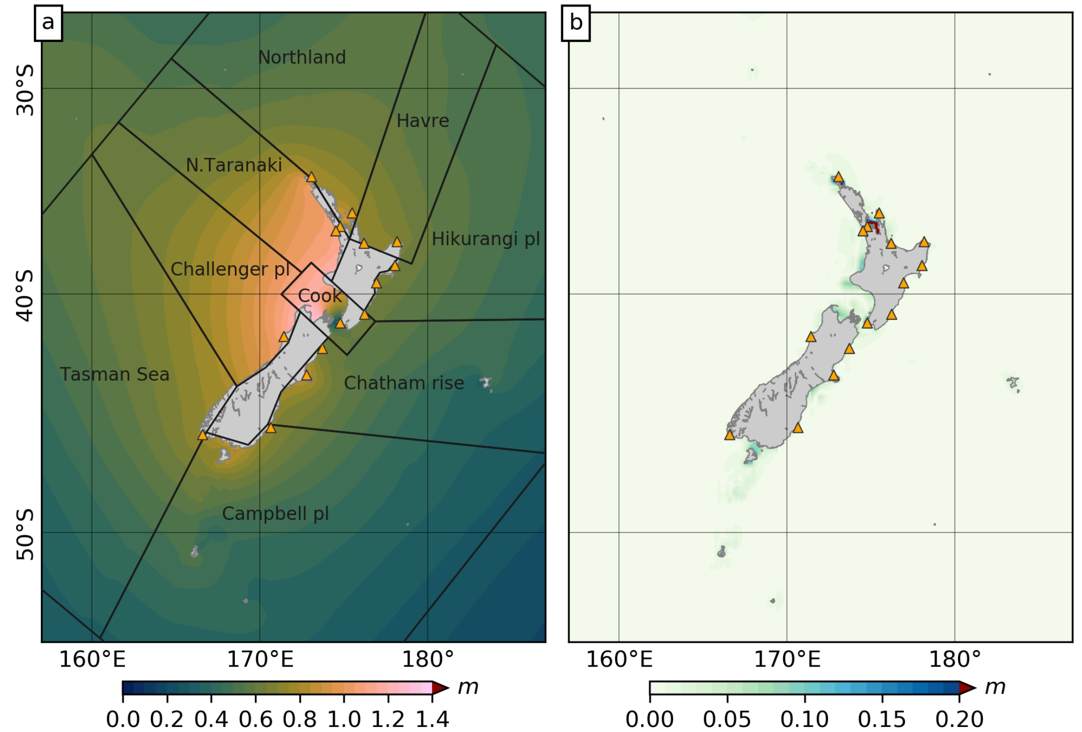

Figure 2. Comparison of recent global ocean tide models (FES2014b, GOT4.10c, TPXO9.v1) around New Zealand: (a) M_2 tidal amplitudes computed as a mean of the ocean tide models. (b) Standard deviation (SD) of the vector differences between the global ocean tide models. The grey labeled polygons in (a) represent the areas used for OTLD phasor reconstruction. Note the scale extension above 0.2 m in (b) to demonstrate the high degree of agreement between these models with exception for ∼1 m SD on one small section of the north coast. Orange triangles represent tide gauges used in the analysis.

3.2 Comparison of GPS and PREM-based Models

The GPS-estimated M_2 up OTLD (with the a priori model restored) are shown in Fig. 3 with horizontal components shown in Fig. S2, and listed in Table S2 for each of the up, north and east components. These show a spatially coherent signal across New Zealand with the amplitude ranging from 2 to 32 mm (sites WAIM and KTIA, respectively). Using these observations and the modeled Z_{OTL} based on FES2014b and PREM we computed Z_{res} as shown in Fig. 4a. M_2 up residuals in the North Island are significant and demonstrate a spatially coherent amplitude of ∼1 mm and phase residual of ∼-10°, while residuals in the South Island are small but harder to interpret due to the lower station density and the low OTLD amplitude (Fig. 1). This is consistent across different global ocean tide models as indicated by the $\|Z_{res}\|$ values summarized in the boxplots (Fig. 4c, S4-5). $\|Z_{res}\|$ variation over the range of tide models with PREM has median value of around 0.7 mm for any of the global tide models while the median for the EEZ model is ∼2 mm. This bias within the EEZ model results in a spatially coherent signal evident from the phasor maps (Fig. S6.2, up component), especially in the North Island.

While all the recent global ocean tide models perform similarly in the horizontal components, FES2014b demonstrates the largest reduction of $\|Z_{res}\|$ over the set of Green's functions in the up component (Fig. S5).

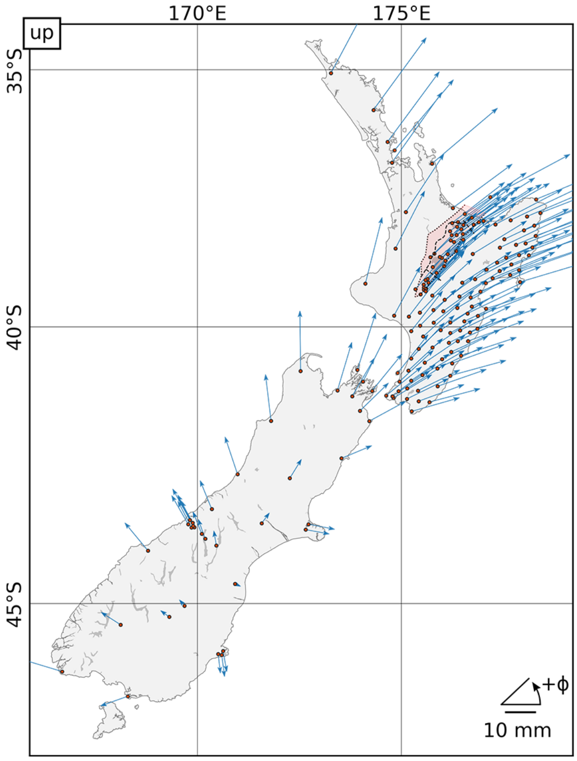

Figure 3. GPS-derived ocean tide loading displacements in the up component. Horizontal components are shown in Fig. S2

using FES2014b with orbits and clocks that were estimated with GOT4.8c may produce results associated with CoM modeling

Note that JPL used the GOT4.8ac tidal model (Desai & Ray, 2014) for OTLD modeling which is inconsistent with the models tested here. This inconsistency may produce results with residuals associated with CoM modeling. Thus we compared modeled results using FES2014b and GOT4.8c and found CoM differences values to be negligible (≤ 0.01 mm). We continue with FES2014b (Fig. 4c) as a baseline ocean tide model for the subsequent tests.

We considered the impact on the total OTLD of specific water bodies by dividing the global oceans into nine separate water areas surrounding New Zealand (Fig. 2). To illustrate the influence of different regions, we selected three sites that experience high, moderate and low M_2 OTLD: KTIA, RGMT and MQZG, respectively (Fig. 5). The set of ocean tide models considered consists of the three recent global atlases (FES2014b, TPXO9.v1 and GOT4.10c), FES2012 and EEZ. The latter produces $\sim$2 mm residual amplitude (purple symbols in Fig. 5) and is, due also to the tide gauge comparison (Table 1), excluded from further analysis. The other models show closer agreement but in general the residuals are larger than the estimated 2-sigma uncertainties of the observed OTLD when using PREM (Fig. 5, bottom panels). However, we note the similar magnitude of the variance in $\|Z_{res}\|$ for all models including EEZ (when the bias is ignored) in the up component and complete absence of a $\|Z_{res}\|$ bias in the horizontal components (Fig. S5).

Residuals using the purely elastic (original with no corrections) STW105 show a similar level of variance and median as PREM (Fig. 4d) while S362ANI shows 50% reduced variance and slightly reduced median (0.48 mm compared with 0.61 mm for PREM). However, neither model produces consistent agreement within the GPS uncertainty as

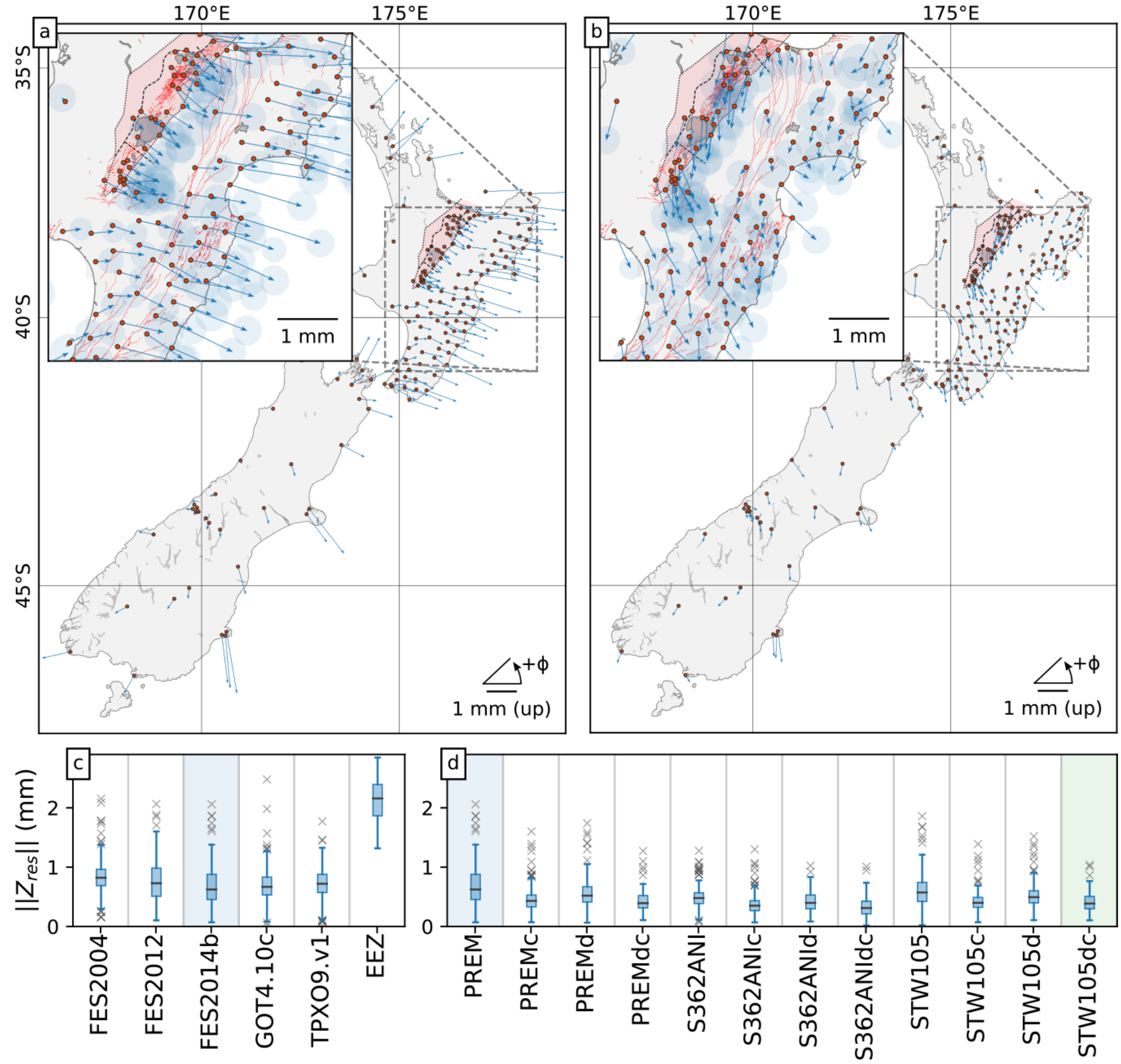

Figure 4. M_2 OTLD residuals relative to FES2014b_PREM (a), FES2014_STW105dc (b) with circles on the ends of phasors representing 95% confidence interval of the derived OTLD values. M_2 OTLD residual magnitude ($\|Z_{res}\|$) boxplots for different model setups (c, d). The horizontal line on each box is the median value, the box represents the inter-quartile range (IQR) and the whiskers show an additional 1.5×IQR. Blue and green shading highlights boxplots of (a) and (b) maps, respectively. The Earth model suffixes 'd' and 'c' in panel (d) refer to the additional treatment of dissipation and compressibility, respectively.

shown, for example, with the three sites presented in Fig. 5. We next explore the sensitivity of the modeled OTLD to anelastic dissipation (denoted suffix "d"), and spatially-varying ocean density and compressibility ("c").

3.3 Effect of Considering Anelasticity (Dissipation)

Bos et al. (2015) demonstrated that accounting for some of the effects of M_2 mantle anelasticity by modifying the Green's functions to include dissipation, decreased OTLD residuals in western Europe by up to 0.2 mm. Matviichuk et al. (2020) confirmed these

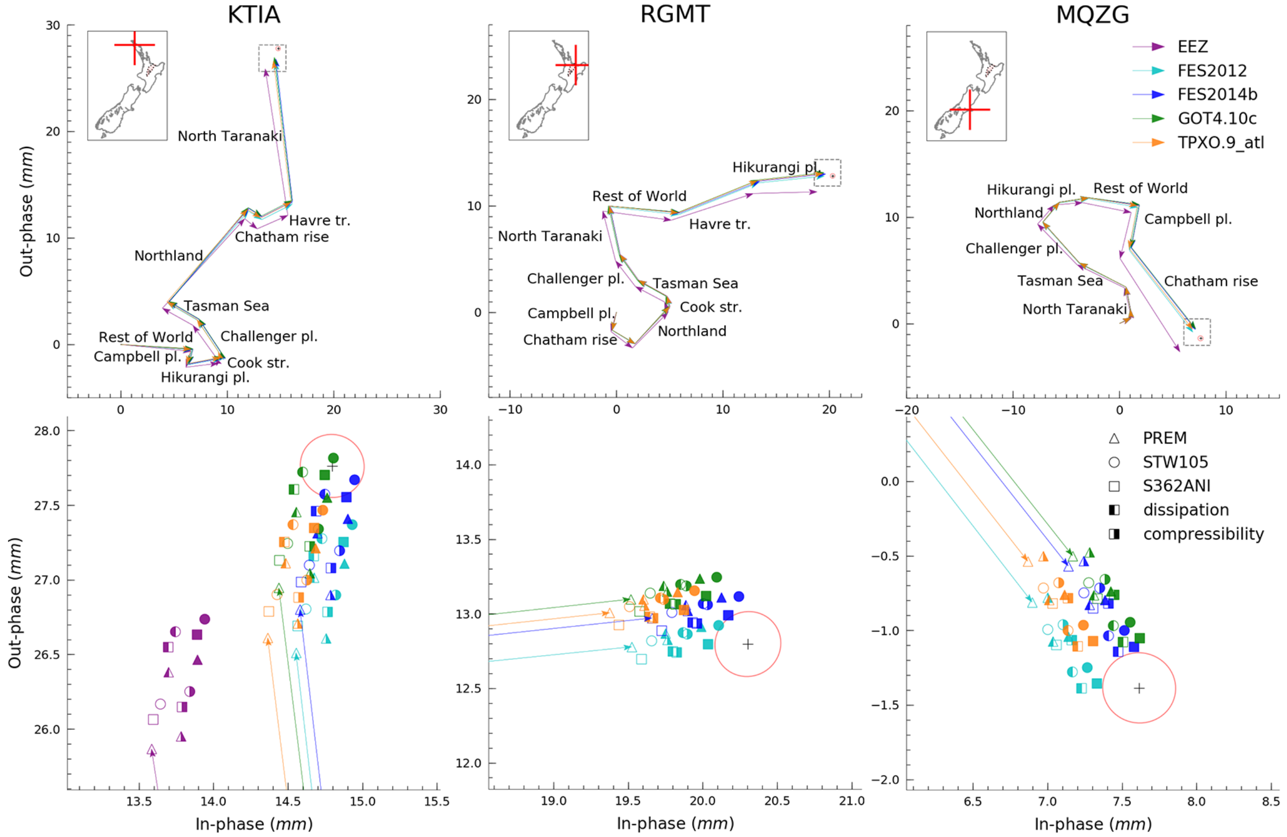

Figure 5. Phasor plots of the OTLD contributions from different oceanic regions (see Fig. 2a) for M_2 Up displacements computed with various Green's functions and ocean tide models. The bottom panels show the detail for the vector tip area shown enclosed by a square in the respective top panels. GPS observations are shown with a black "+" and 95% confidence interval as a red circle. OTLD produced by the are outside the polygons shown in Fig. 2a is titled as "rest of the world".

Table 1. Average M_2 amplitude differences computed over 15 tide gauges relative to a set of ocean tide models.

	FES2004	FES2012	FES2014b	GOT4.10c	TPXO.9_atl	EEZ
Avg. difference (cm)	-0.81	2.95	3.05	1.13	2.32	8.41

results for the same region but using a different time frame, while similar results have been found by Wang et al. (2020) and Martens and Simons (2020) for south-east Asia and Alaska, respectively.

For New Zealand, we find a reduction of $\|Z_{res}\|$ variance and median for all Earth models when dissipation is included (Fig. 4d). The effect is illustrated in Fig. 5 where the models including dissipation (squares with left side only filled) are shown to be closer to the GPS estimates. These do, however, remain outside the GPS 95% confidence interval. At the same time as this improvement, we noticed the introduction of up to 0.2 mm $\|Z_{res}\|$ bias into the north component with dissipation enabled, independent of the Green's function used; the east component also shows this effect but only with S362ANI

(Fig. S4). Enabling sea water compressibility correction partially suppresses the bias. We discuss this further below.

3.4 Assessment of Water Density and Compressibility Correction

Enabling the seawater compressibility correction decreases the median $\|Z_{res}\|$ by a further ~0.2 mm in the up component, as shown in Fig. 4d and by example in Fig. 5 (fully filled symbols). In some cases, the application of both dissipation and compressibility eliminates the residual in the up component, although as we discuss in the next section, large, regionally coherent residuals persist. Horizontal components show an increase in variance (Fig. S4) with only compressibility considered. The dissipation-introduced $\|Z_{res}\|$ bias in the north component can be partially (S362ANIdc) or completely (PREMdc, STW105dc) removed by additionally applying the compressibilty correction (Fig. S4-5, FES2014b). The east component shows a marginal (less than 0.1 mm) increase in both $\|Z_{res}\|$ median and variance over the solutions with just dissipation included for PREM and STW105, while S362ANI shows further dissipation-introduced increase in $\|Z_{res}\|$ bias by another 0.1 mm (Fig. S4).

Following Martens and Simons (2020), we constructed Empirical Cumulative Distribution Function (ECDF) plots (Fig. S7.1) to investigate the impact of corrections on the distribution of $\|Z_{res}\|$. The ECDF analysis shows the expected behavior of the corrections in the up component: each correction increases the slope of the ECDF indicating successive improvement with each correction. This is not the case for the horizontal components where both corrections introduce biases using S362ANI, which otherwise demonstrates performance comparable to other models without the corrections. The optimum correction of PREM and STW105 in the north component very much relies on the selection of ocean tide model. The dissipation-introduced bias is suppressed by the compressibility correction in the case of FES2014b and GOT4.10c, which suggests the best performance with both dissipation and compressibility corrections enabled. In the case of TPXO9.v1, the bias is too large for compressibility to overcome, effectively repeating the trend as observed for S362ANI.

Removing the respective mean Z_{res} values from each set of residuals (Fig. S7.2) aligns the ECDFs over all components, fully removing the differences in the horizontal components with exception for S362ANI-based values in the north component. Removing mean Z_{res} also absorbs any long-wavelength errors incurred through any mismodeling of the solid Earth body tide.

4 Discussion

Following these tests, the optimal agreement between the observed and modeled OTLD in all three components occurs when using FES2014b and STW105dc. The spatial distribution of Z_{res} shows a spatially coherent signal with amplitude of ~0.5 mm over the Taupo Volcanic Zone (TVZ) in the North Island, as shown in Fig. 4. The dense coverage of stations in these regions reveals a distinct change of Z_{res} between sites in the East Coast (EC) and TVZ that experience the same M_2 OTLD (Fig. 1).

To aid discussion, we consider four different regions (blocks) within this region as illustrated by the symbols in Fig. 6: TVZc, TVZs, ECc, ECs, with "c" and "s" subscripts identifying central and southern subareas, respectively. Residual OTLD in each block was averaged to provide Z_{res} summary metrics (per component) relevant to each region (Table S6). Note that several sites along the EC were removed (e.g. Hawke Bay) as they experience a localized signal caused mainly by the unmodeled ocean tides (Fig. 6, black symbols) which is independent of the ocean tide model or Green's function used. The sites in both TVZ regions show residual amplitudes of ~0.5 mm with phase changing sharply from -102° to -70° between TVZc and TVZs. The relative phase change between TVZ and EC within the same central or south area (TVZc/ECc and TVZs/ECs) is found to be approximately constant (∼35°) while revealing 0.25 mm and 0.15 mm larger amplitudes for TVZc and TVZs, respectively.

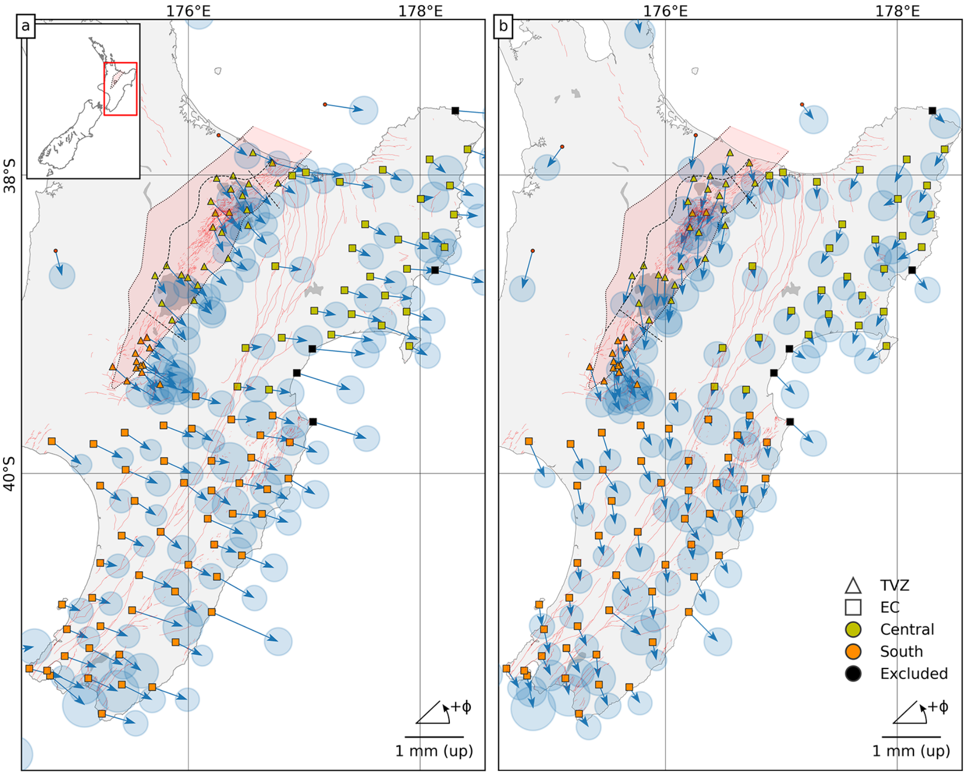

Figure 6. GPS-derived M_2 OTLD residuals for a section of the North Island relative to FES2014b ocean tide model combined with dissipation corrected STW105d (a) and STW105dc (b). "d" and "c" suffixes stand for dissipation and compressibility corrections. Sites are categorized into Taupo Volcanic Zone (TVZ) and East Coast (EC) regions (symbol shape) with subdivision of each into central and south along the TVZ central/south boundary (symbol color). Circles on the ends of phasors represent 95% confidence interval of the derived OTLD residuals

The sharp change in residual phase between TVZc and TVZs, and the strong spatial variation in residual amplitude between respective EC and TVZ sub-regions over length-scales of the order of ∼100 km suggests that the variations are due to localized effects. We discount errors in ocean tides given our previous tests and the spatial distribution of the residuals. Also, biases in the adopted deep Earth rheological structure (Lau et al., 2017) would be effectively constant over this spatial scale.

Instead, our assumption is that the residuals result from mismodeled shallow-Earth rheological structure. To explore this further, we iterate through a range of alternative Earth models, all one-dimensional but with different rheological structure in the upper tens of kilometers based on seismic tomography inversions (Eberhart-Phillips & Bannister, 2015; Eberhart-Phillips & Fry, 2018). No single one-dimensional (radially-varying) Earth model could explain the regional pattern of residuals, with changes generally producing changes that were spatially uniform across the region of Fig. 6.

Deviations in the shallow rheological structure from that used to compute the Earth body tides could produce localized residuals. Zürn et al. (1976) developed a 2D finite-element model of a subduction zone in Alaska, and showed that the subduction zone structure can produce an effect up to 0.8% on the solid Earth body tide in the radial direction directly above the asthenospheric slab. For the M_2 body tide at the latitude of the

North Island, this equates to 0.7 mm. However, their modeling also showed that the maximum gradient in the body tide over the distance from East coast to the TVZ (up to 150 km) should not exceed 0.25% (Zürn et al., 1976, Fig. 5). We note that the effect on phase is not described in their work. However, if we consider the relative location of the TVZ over the subduction slab (observed by the Vp anomaly at 100-130 km depth (Eberhart-Phillips & Fry, 2018)), the maximum expected change becomes close to 0.15%, or 0.13 mm for M_2 at these latitudes. As such, this is well below the magnitude of the variations seen in Fig. 6.

The effect of lateral rheological structure on modeled OTLD is unclear. However, modeling of elastic deformation due to longer-period surface mass displacement indicates that consideration of localized Earth structure produced differences of the order 10% in the vertical and 20% in the horizontal over distances of 10-50 km (Dill et al., 2015). The average M_2 OTLD in the region of the TVZ shown in Fig. 6 is $\sim$19 mm and so even a 2% effect due to lateral variation may be relevant to explaining the observed residuals. Given the minor, but non-negligible effect of lateral variation on Earth body tides, and likely effects on OTLD, our analysis suggests that one-dimensional models of this region are unlikely to fully explain GPS observations of OTLD at M_2. To check for potential long-wavelength errors that could introduce the observed dissipation-introduced biases in the horizontal components, we repeated our analyses for a set of 15 stations in inland Australia (see Table S3 for site list and Table S4 for derived observations) where the geological setting is simpler and where a 1D model should produce accurate results. For this dataset we needed to adopt a different time period (2015-2018 inclusive) due to data availability but checking a subset of sites in New Zealand found that the time-period was inconsequential. Figures S9 and S10 demonstrate that, although the magnitude of the OTLD is still several mm, for these stations the residuals (observed minus predicted OTLD) are indeed small and within the uncertainty of the observations. This validates the robustness of our analyses and suggests that tidal centre-of-mass errors in this region are small, specifically for FES2014b and GOT4.10c ocean tide models.

Figures S7.1 and S7.2 show that the OTLD residuals for the horizontal components suffer from a common mode issue that modification of the Green's function cannot overcome. For the up component, the influence of the dissipation effect within asthenosphere that requires us to modify the elastic properties of the Earth model from the reference period of 1s to tidal periods is noticeable. Furthermore, including spatially varying seawater density and compressibility results in an additional reduction of the misfit. These two figures also demonstrate that the difference between the ocean tide models used in the loading computations is small. Therefore, the most likely candidate to reduce the misfit further is to use an advanced (3D) (an)elastic model of the region.

Similar problems using a 1D Earth modeling OTLD in Alaska were recently described by Martens and Simons (2020). We are unaware of three-dimensional models being in use for the computation of OTLD, however Latychev et al. (2009) have computed Earth body tides with a three-dimensional model. One practical consequence of this is that mismodeled tidal deformations in this region will propagate into conventional 24 hr coordinate solutions (Penna et al., 2007). Such propagation will introduce long-period noise in GPS coordinate time series in New Zealand and impact subsequent geophysical interpretation.

5 Conclusions

We estimate M_2 ocean tide loading displacements (OTLD) at 170 GPS sites in New Zealand from the beginning of 2013 to mid-2020 (doy 153). Comparison with modeled OTLD displacements using a range of global tide models and elastic PREM shows sub-mm agreement, with much larger disagreements when using a local New Zealand tide model.

However, on close inspection we find that no single one-dimensional elastic Earth model, when combined with modern global tide models, can consistently explain the GPS-derived OTLD within uncertainties. Of the tested ocean tide models, FES2014b produced the best results. However, application of an anelastic dissipation correction, and varying water density and compressibility substantially improves the agreement between the various models and observed OTLD. Despite this, some regional spatially-coherent unmodeled residual signals remain in the North Island with magnitudes of up to 0.3 mm. These show substantial variation in phase over ∼100 km in the region between the Taupo Volcanic Zone and the East coast. We attempted to reproduce the observed signal using a range of 1D Earth models with varying shallow Earth structures, including the effects of anelasticity, however no single model could explain the residuals. We anticipate that these residuals are a result of unmodeled lateral variations in Earth rheological structure forced largely by ocean tide loading but with a smaller component likely from mismodeled Earth body tides.

This analysis of residual OTLD demonstrates the deficiencies of the 1D Earth modeling approach that is currently standard practice. This is particularly relevant to GPS analysis using 24 hr coordinate solutions, given mismodeled tidal displacements propagate into long-period signal. Utilizing 3D Earth modeling to compute tidal phenomena is likely required to explain the observations in regions with major discontinuities in Earth's lateral structure (e.g. subduction margins). Such models, combined with these observations, could provide new insights into the shallow rheological structure of these regions.

Acknowledgments

We greatly acknowledge the New Zealand GeoNet project and its sponsors EQC, GNS Science and LINZ, and Geoscience Australia for providing the data used in this study. We are grateful to NASA Jet Propulsion Laboratory for GipsyX software, products and support. The services of TPAC High Performance Computing Facility are acknowledged gratefully. We thank Klaus Schueller for advice and discussion on Eterna software. We acknowledge the support of Elisabetta D'Anastasio in accessing the data and site logs.

Bogdan Matviichuk is supported by Tasmania Graduate Research Scholarship. MSB is supported by the project FCT/UIDB/50019/2020 – IDL funded by FCT.

GipsyX binaries were provided under license from JPL. Eterna tidal analysis and prediction software with source code was acquired from International Geodynamics and Earth Tide Service (IGETS), `igets.u-strasbg.fr/soft_and_tool.php`. The RINEX files can be acquired from `ftp.geonet.org.nz`, coordinate time series are provided at `data.utas.edu.au/metadata/ff80025e-0019-4cbb-aa8a-2fb289915b51`. Figures 1 and 2 use perceptually uniform color maps of Crameri et al. (2020).

References

Abbaszadeh, M., Clarke, P. J., & Penna, N. T. (2020). Benefits of combining GPS and GLONASS for measuring ocean tide loading displacement. *Journal of Geodesy*, *94*(7), 63. doi: 10.1007/s00190-020-01393-5

Alterman, Z., Jarosch, H., Pekeris, C. L., & Jeffreys, H. (1959). Oscillations of the earth. *Proceedings of the Royal Society of London. Series A. Mathematical and Physical Sciences*, *252*(1268), 80–95. doi: 10.1098/rspa.1959.0138

Bertiger, W., Bar-Sever, Y., Dorsey, A., Haines, B., Harvey, N., Hemberger, D., ... Willis, P. (2020). GipsyX/RTGx, a new tool set for space geodetic operations and research. *Advances in Space Research*, *66*(3), 469–489. doi: 10.1016/j.asr.2020.04.015

Bertiger, W., Desai, S. D., Haines, B., Harvey, N., Moore, A. W., Owen, S., & Weiss, J. P. (2010). Single receiver phase ambiguity resolution with GPS data. *Journal of Geodesy*, *84*(5), 327–337. doi: 10.1007/s00190-010-0371-9

Bos, M. S., & Baker, T. F. (2005). An estimate of the errors in gravity ocean tide loading computations. *Journal of Geodesy*, *79*(1), 50–63. doi: 10.1007/s00190

-005-0442-5
Bos, M. S., Penna, N. T., Baker, T. F., & Clarke, P. J. (2015). Ocean tide loading displacements in western europe: 2. gps-observed anelastic dispersion in the asthenosphere. *Journal of Geophysical Research: Solid Earth*, *120*(9), 6540–6557. doi: 10.1002/2015JB011884
Bos, M. S., & Scherneck, H.-G. (2013). Computation of Green's Functions for Ocean Tide Loading. In G. Xu (Ed.), *Sciences of Geodesy - II* (pp. 1–52). Berlin, Heidelberg: Springer Berlin Heidelberg. doi: 10.1007/978-3-642-28000-9_1
Carrere, L., Lyard, F., Cancet, M., Guillot, A., & Dupuy, S. (2016). Fes 2014 : a new global tidal model. , 8.
Carrere, L., Lyard, F., Cancet, M., Guillot, A., & Roblou, L. (2013). Fes 2012: A new global tidal model taking advantage of nearly 20 years of altimetry. In *20 years of progress in radar altimetry* (Vol. 710, p. 13).
Crameri, F., Shephard, G. E., & Heron, P. J. (2020). The misuse of colour in science communication. *Nature Communications*, *11*, 5444. doi: 10.1038/s41467-020-19160-7
Desai, S. D., & Ray, R. D. (2014). Consideration of tidal variations in the geocenter on satellite altimeter observations of ocean tides. *Geophysical Research Letters*, *41*(7), 2454–2459. doi: 10.1002/2014GL059614
Dill, R., Klemann, V., Martinec, Z., & Tesauro, M. (2015). Applying local green's functions to study the influence of the crustal structure on hydrological loading displacements. *Journal of Geodynamics*, *88*, 14–22. doi: 10.1016/j.jog.2015.04.005
Dziewonski, A. M., & Anderson, D. L. (1981). Preliminary reference earth model. *Physics of the Earth and Planetary Interiors*, *25*(4), 297–356. doi: 10.1016/0031-9201(81)90046-7
Eberhart-Phillips, D., & Bannister, S. (2015). 3-D imaging of the northern Hikurangi subduction zone, New Zealand: variations in subducted sediment, slab fluids and slow slip. *Geophysical Journal International*, *201*(2), 838–855. doi: 10.1093/gji/ggv057
Eberhart-Phillips, D., & Fry, B. (2018). Joint local earthquake and teleseismic inversion for 3-D velocity and Q in New Zealand. *Physics of the Earth and Planetary Interiors*, *283*, 48–66. doi: 10.1016/j.pepi.2018.08.005
Egbert, G. D., & Erofeeva, S. Y. (2002). Efficient Inverse Modeling of Barotropic Ocean Tides. *Journal of Atmospheric and Oceanic Technology*, *19*(2), 183–204. doi: 10.1175/1520-0426(2002)019⟨0183:EIMOBO⟩2.0.CO;2
Farrell, W. E. (1972a). Deformation of the earth by surface loads. *Reviews of Geophysics*, *10*(3), 761–797. doi: 10.1029/RG010i003p00761
Farrell, W. E. (1972b). Global Calculations of Tidal Loading. *Nature Physical Science*, *238*(81), 43–44. doi: 10.1038/physci238043a0
Gale, N., Gledhill, K., Chadwick, M., & Wallace, L. (2015). The Hikurangi Margin Continuous GNSS and Seismograph Network of New Zealand. *Seismological Research Letters*, *86*(1), 101–108. doi: 10.1785/0220130181
Guo, J.-Y., Ning, J.-S., & Zhang, F.-P. (2001). Chebyshev-collocation method applied to solve odes in geophysics singular at the earth center. *Geophysical Research Letters*, *28*(15), 3027–3030. doi: 10.1029/2001GL012886
Hu, Y., Bürgmann, R., Banerjee, P., Feng, L., Hill, E. M., Ito, T., … Wang, K. (2016). Asthenosphere rheology inferred from observations of the 2012 indian ocean earthquake. *Nature*, *538*(7625), 368–372. doi: 10.1038/nature19787
Ito, T., & Simons, M. (2011). Probing asthenospheric density, temperature, and elastic moduli below the western united states. *Science*, *332*(6032), 947–951. doi: 10.1126/science.1202584
Karato, S.-i. (2012). On the origin of the asthenosphere. *Earth and Planetary Science Letters*, *321-322*, 95–103. doi: 10.1016/j.epsl.2012.01.001
Kustowski, B., Ekström, G., & Dziewoński, A. M. (2008). Anisotropic shear-wave

velocity structure of the earth's mantle: A global model. *Journal of Geophysical Research: Solid Earth*, *113*(B6). doi: 10.1029/2007JB005169
Lamarche, G., & Lebrun, J.-F. (2000). Transition from strike-slip faulting to oblique subduction: active tectonics at the puysegur margin, south new zealand. *Tectonophysics*, *316*(1), 67–89. doi: 10.1016/S0040-1951(99)00232-2
Latychev, K., Mitrovica, J. X., Ishii, M., Chan, N.-H., & Davis, J. L. (2009). Body tides on a 3-D elastic earth: Toward a tidal tomography. *Earth and Planetary Science Letters*, *277*(1), 86–90. doi: 10.1016/j.epsl.2008.10.008
Lau, H. C. P., Mitrovica, J. X., Davis, J. L., Tromp, J., Yang, H.-Y., & Al-Attar, D. (2017). Tidal tomography constrains Earth's deep-mantle buoyancy. *Nature*, *551*(7680), 321–326. doi: 10.1038/nature24452
Lyard, F., Lefevre, F., Letellier, T., & Francis, O. (2006). Modelling the global ocean tides: modern insights from FES2004. *Ocean Dynamics*, *56*(5-6), 394–415. doi: 10.1007/s10236-006-0086-x
Martens, H. R., & Simons, M. (2020). A comparison of predicted and observed ocean tidal loading in alaska. *Geophysical Journal International*, ggaa323. doi: 10.1093/gji/ggaa323
Martens, H. R., Simons, M., Owen, S., & Rivera, L. (2016). Observations of ocean tidal load response in south america from subdaily gps positions. *Geophysical Journal International*, *205*(3), 1637–1664. doi: 10.1093/gji/ggw087
Matviichuk, B. (2020). *GipsyX Wrapper: v0.1.0.* doi: 10.5281/zenodo.4001166
Matviichuk, B., King, M., & Watson, C. (2020). Estimating ocean tide loading displacements with GPS and GLONASS. *Solid Earth*, *11*(5), 1849–1863. doi: 10.5194/se-11-1849-2020
Penna, N. T., Clarke, P. J., Bos, M. S., & Baker, T. F. (2015). Ocean tide loading displacements in western europe: 1. validation of kinematic gps estimates. *Journal of Geophysical Research: Solid Earth*, *120*(9), 6523–6539. doi: 10.1002/2015JB011882
Penna, N. T., King, M. A., & Stewart, M. P. (2007). Gps height time series: Short-period origins of spurious long-period signals. *Journal of Geophysical Research: Solid Earth*, *112*(B2). doi: 10.1029/2005JB004047
Petit, G., & Luzum, B. (2010). IERS Conventions (2010). (36), 179.
Ray, R. D. (2013). Precise comparisons of bottom-pressure and altimetric ocean tides: Bottom-pressure and altimetric tides. *Journal of Geophysical Research: Oceans*, *118*(9), 4570–4584. doi: 10.1002/jgrc.20336
Stammer, D., Ray, R. D., Andersen, O. B., Arbic, B. K., Bosch, W., Carrère, L., … Yi, Y. (2014). Accuracy assessment of global barotropic ocean tide models. *Reviews of Geophysics*, *52*(3), 243–282. doi: 10.1002/2014RG000450
Stern, R. (2004). Subduction initiation: spontaneous and induced. *Earth and Planetary Science Letters*, *226*(3-4), 275–292. doi: 10.1016/S0012-821X(04)00498-4
Walters, R. A., Goring, D. G., & Bell, R. G. (2001). Ocean tides around New Zealand. *New Zealand Journal of Marine and Freshwater Research*, *35*(3), 567–579. doi: 10.1080/00288330.2001.9517023
Wang, J., Penna, N. T., Clarke, P. J., & Bos, M. S. (2020). Asthenospheric anelasticity effects on ocean tide loading around the east china sea observed with gps. *Solid Earth*, *11*(1), 185–197. doi: 10.5194/se-11-185-2020
Wenzel, H.-G. (1996). The nanogal software : Earth tide data processing package ETERNA 3.30. *Bull. Inf. Marées Terrestres*, *124*, 9425–9439.
Wessel, P., & Smith, W. H. F. (1996). A global, self-consistent, hierarchical, high-resolution shoreline database. *Journal of Geophysical Research: Solid Earth*, *101*(B4), 8741–8743. doi: 10.1029/96JB00104
Yuan, L., & Chao, B. F. (2012). Analysis of tidal signals in surface displacement measured by a dense continuous gps array. *Earth and Planetary Science Letters*, *355-356*, 255–261. doi: 10.1016/j.epsl.2012.08.035
Yuan, L., Chao, B. F., Ding, X., & Zhong, P. (2013). The tidal displacement field at

earth's surface determined using global gps observations: Tidal displacements determined by gps. *Journal of Geophysical Research: Solid Earth*, *118*(5), 2618–2632. doi: 10.1002/jgrb.50159

Zumberge, J. F., Heflin, M. B., Jefferson, D. C., Watkins, M. M., & Webb, F. H. (1997). Precise point positioning for the efficient and robust analysis of gps data from large networks. *Journal of Geophysical Research: Solid Earth*, *102*(B3), 5005–5017. doi: 10.1029/96JB03860

Zweng, M. M., Reagan, J. R., Antonov, J. I., Locarnini, R. A., Mishonov, A. V., Boyer, T. P., ... Levitus, S. (2013). World ocean atlas 2013. Volume 2, Salinity.. doi: 10.7289/V5251G4D

Zürn, W., Beaumont, C., & Slichter, L. B. (1976). Gravity tides and ocean loading in southern alaska. *Journal of Geophysical Research (1896-1977)*, *81*(26), 4923–4932. doi: 10.1029/JB081i026p04923

Supporting Information for "Limitations in one-dimensional (an)elastic Earth models for explaining GPS-observed M_2 Ocean Tide Loading displacements in New Zealand"

B. Matviichuk[1], M. King[1],C. Watson[1], M. Bos[2]

[1]School of Geography, Planning, and Spatial Sciences, University of Tasmania, Hobart, 7001, Australia

[2]Instituto Dom Luiz (IDL), University of Beira Interior, Covilhã, Portugal

Contents of this file

1. Figures S1 to S10
2. Table S5
3. Table S6

Additional Supporting Information (Files uploaded separately)

1. Table S1. New Zealand GPS site name, network and coordinates (Table_S1.xlsx)
2. Table S2. New Zealand GPS-derived M_2 amplitudes and phases (Table_S2.xlsx)
3. Table S3. Australia GPS site name, network and coordinates (Table_S3.xlsx)
4. Table S4. Australia GPS-derived M_2 amplitudes and phases (Table_S4.xlsx)

0148-0227/21/$9.00

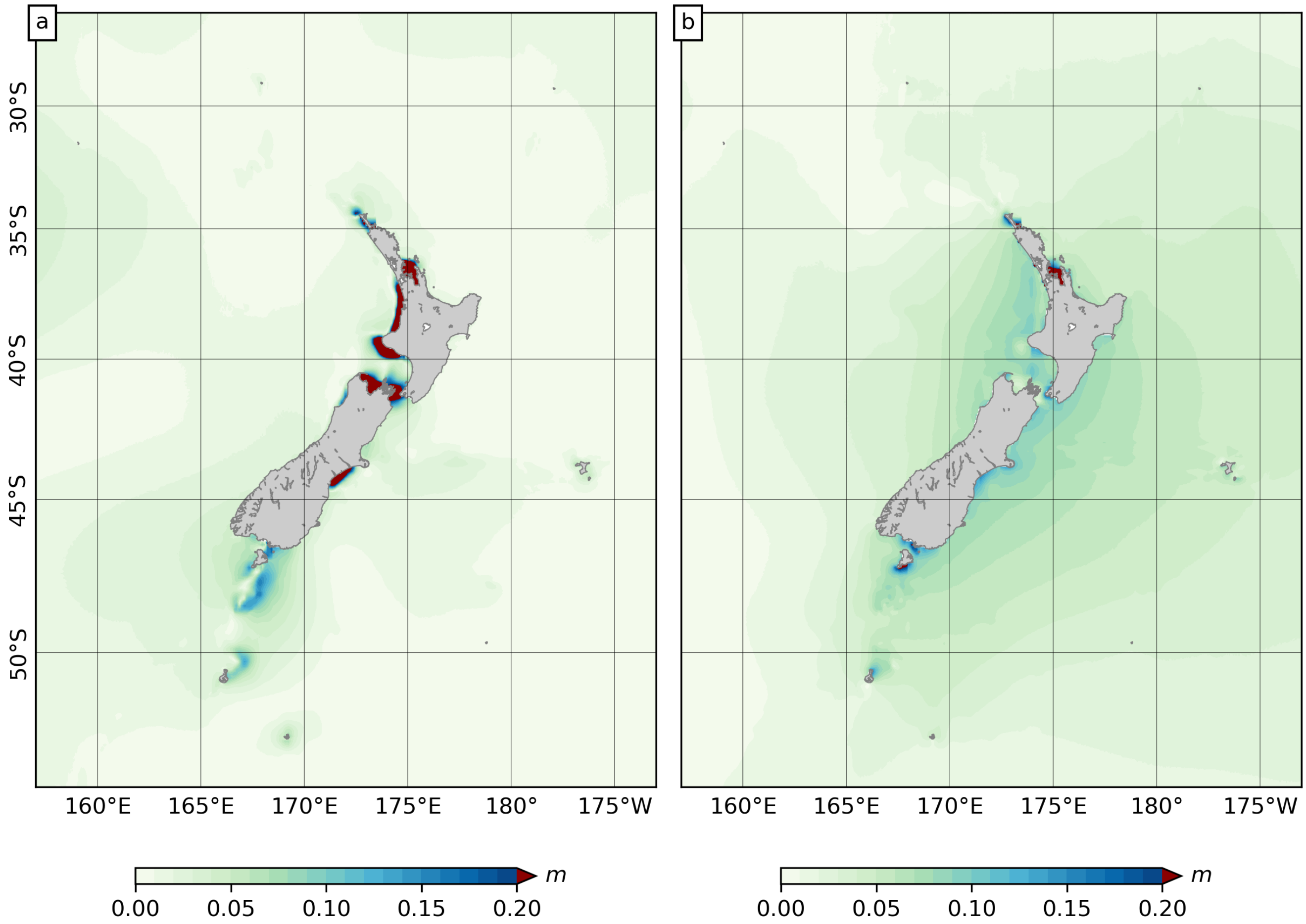

Figure S1. Vector differences between the mean model and FES2004 global tide model (a) and regional EEZ ocean tide model (b). Differences are concentrated in the shallow waters in the case of FES2004 while EEZ differences show the presence of uniform bias (∼0.1 m), which reduces away from the coast. Note the scale saturation above 0.2 m. The peak values are 1 m and 0.7 m for (a) and (b), located at the Hauraki Gulf in both cases.

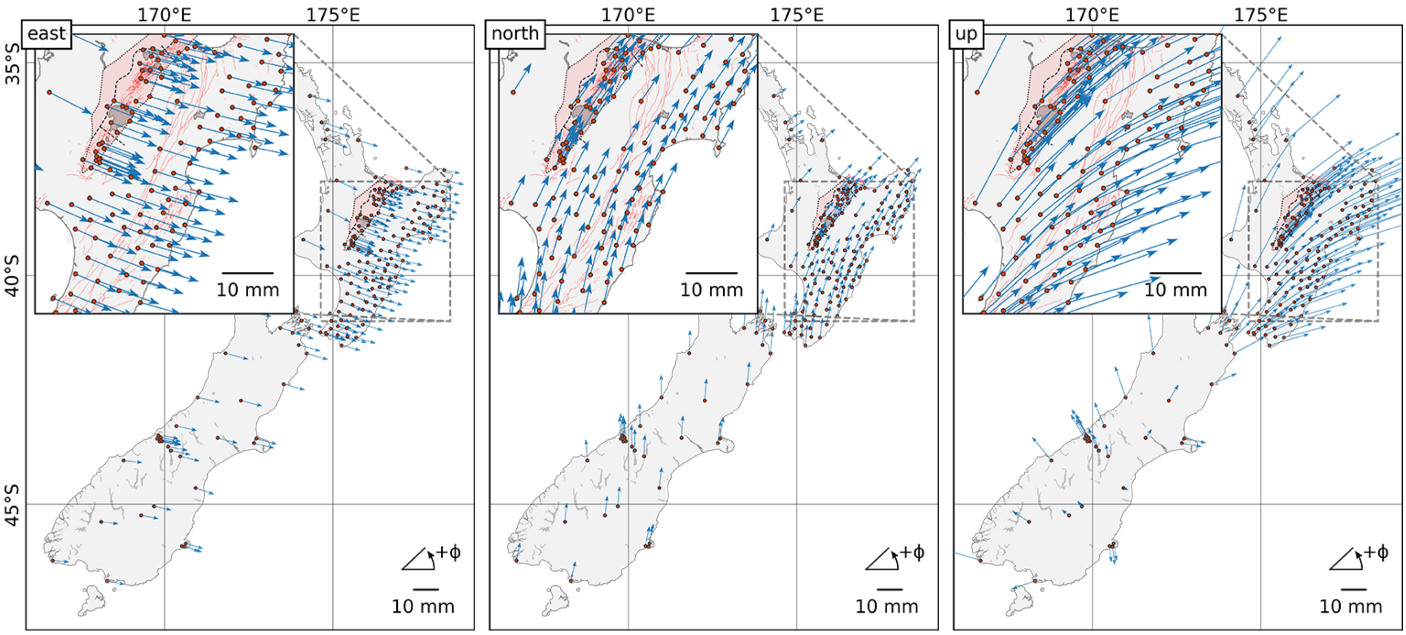

Figure S2. FES2004 restored GPS-derived ocean tide loading in the east, north and up components.

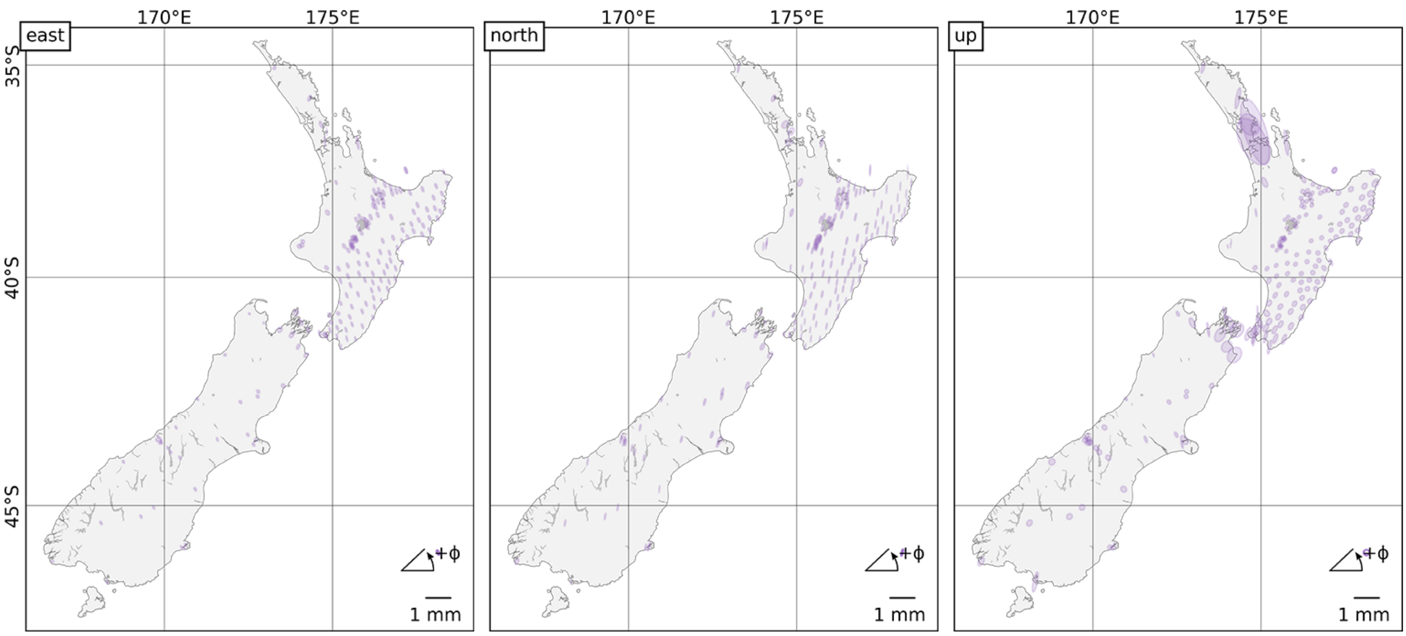

Figure S3. Influence of errors in the ocean-tide models on the modeled OTL values shown as 95% confidence ellipsoids of vector differences between OTL values based on FES2014b, TPXO9.v1 and GOT4.10c ocean tide models. The Green's function was kept fixed to STW105d. The errors were computed separately for in-phase and out-phase components. The scale is consistent with the rest of OTL residuals maps.

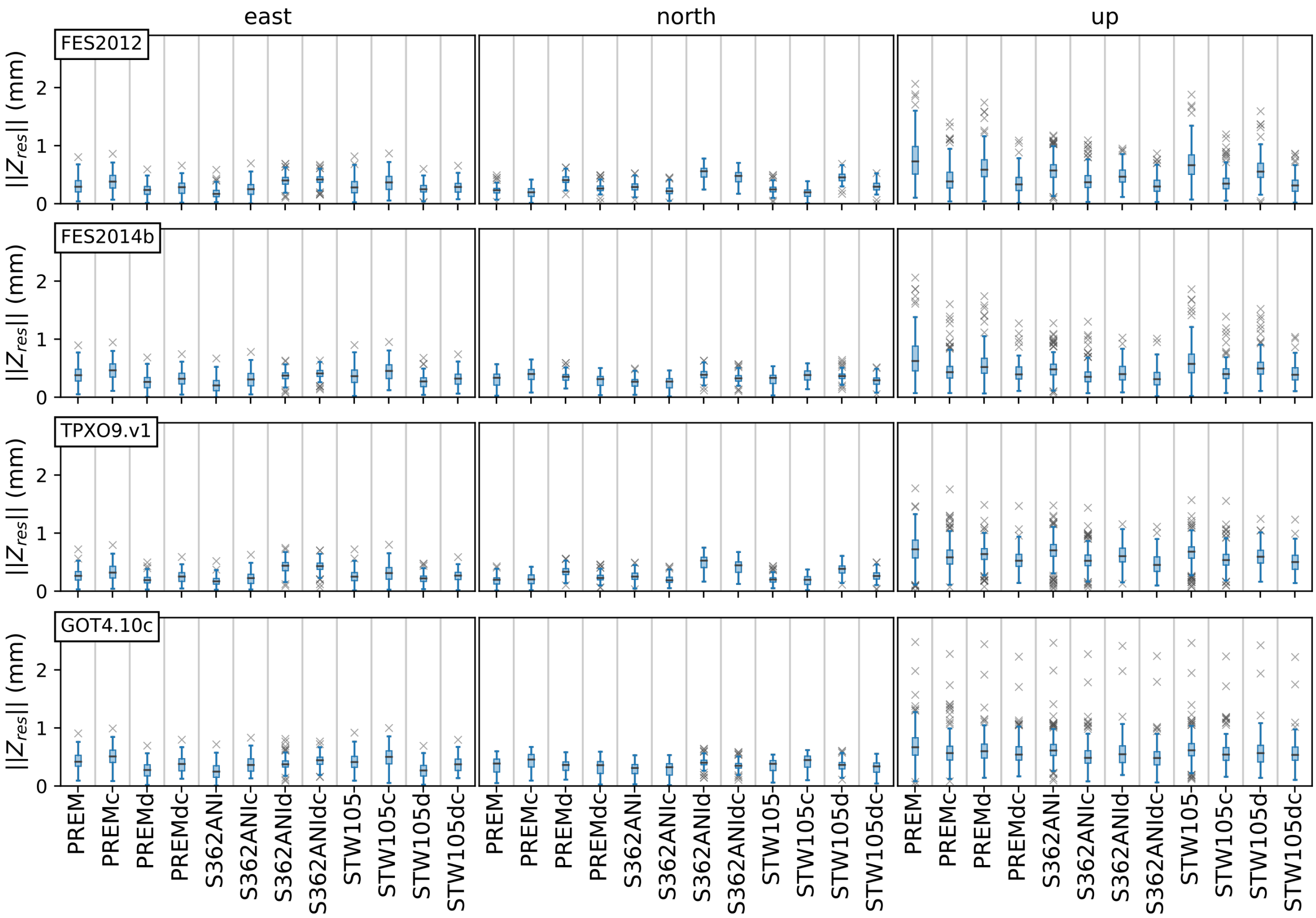

Figure S4. Residual OTL, $\|Z_{res}\|$, relative to (top to bottom) FES2012, FES2014b, TPXO9.v1, GOT4.10c ocean tide models and a set of Green's functions for the east, north and up components (left to right).

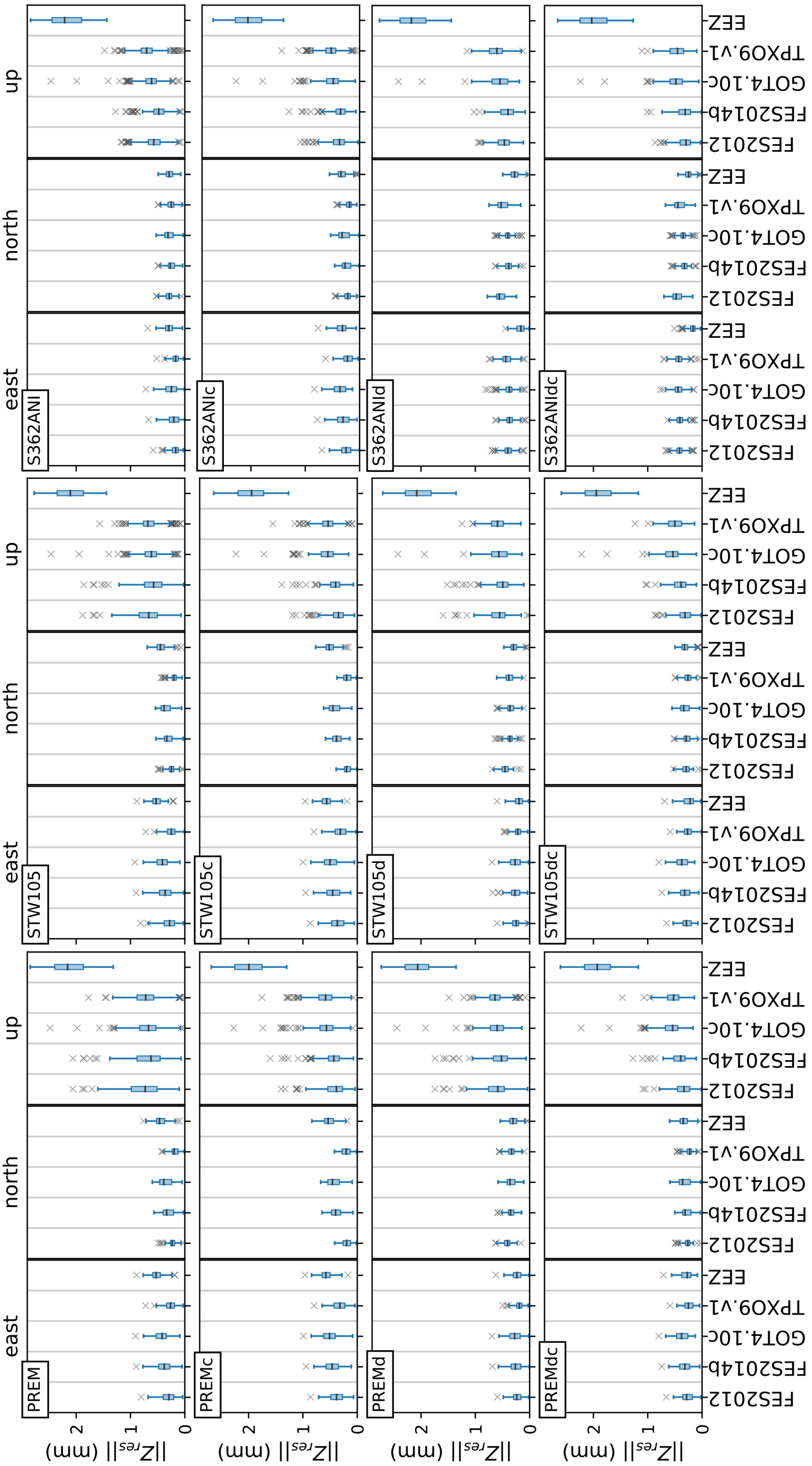

Figure S5. Comparison of FES2012, FES2014b, TPXO9.v1 and GOT4.10c ocean tide models over a range of Green's functions and corrections of compressibility and dissipation.

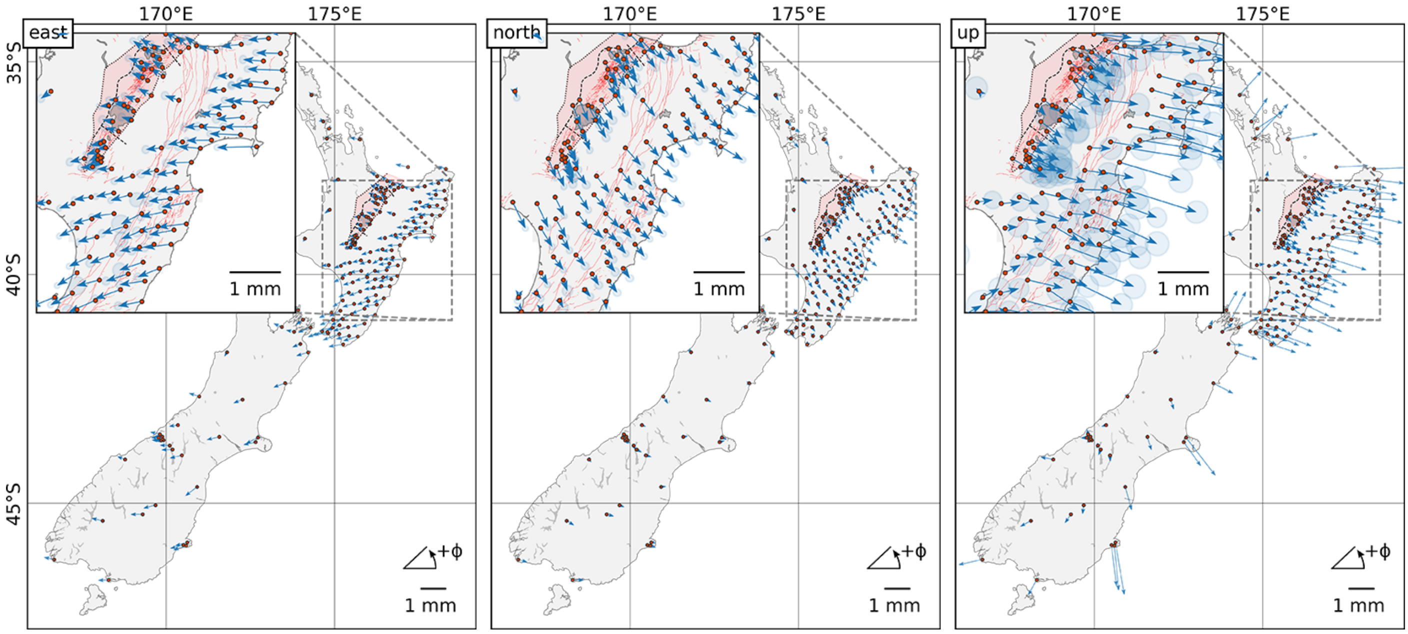

Figure S6.1. Residual OTL, $\|Z_{res}\|$, relative to FES2014b ocean tide model and PREM Green's function in the east, north and up components.

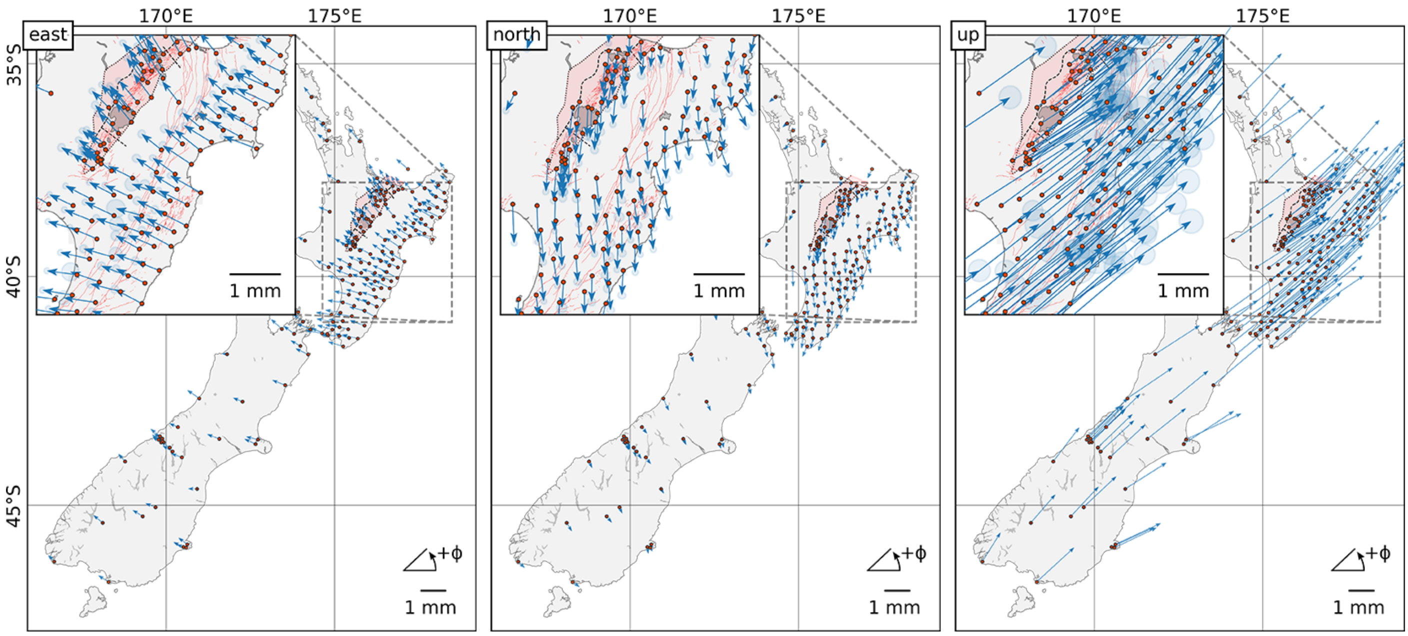

Figure S6.2. Residual OTL, $\|Z_{res}\|$, relative to EEZ regional ocean tide model (FES2014b outside EEZ's coverage) and PREM Green's function in the east, north and up components.

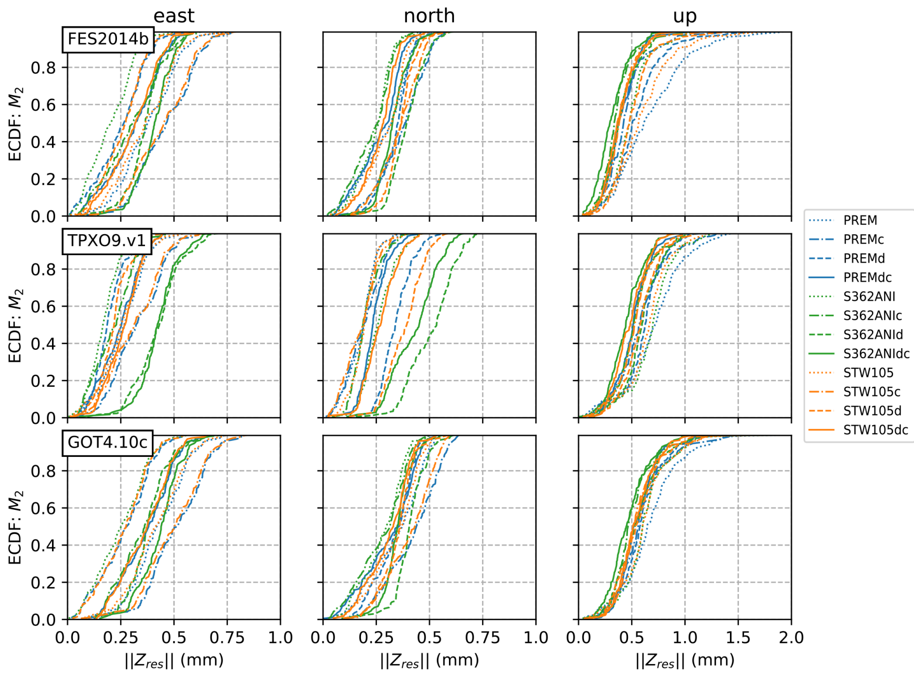

Figure S7.1. ECDF plots for three recent global ocean tide models ocean tide models and a set of Green's functions for the east, north and up components.

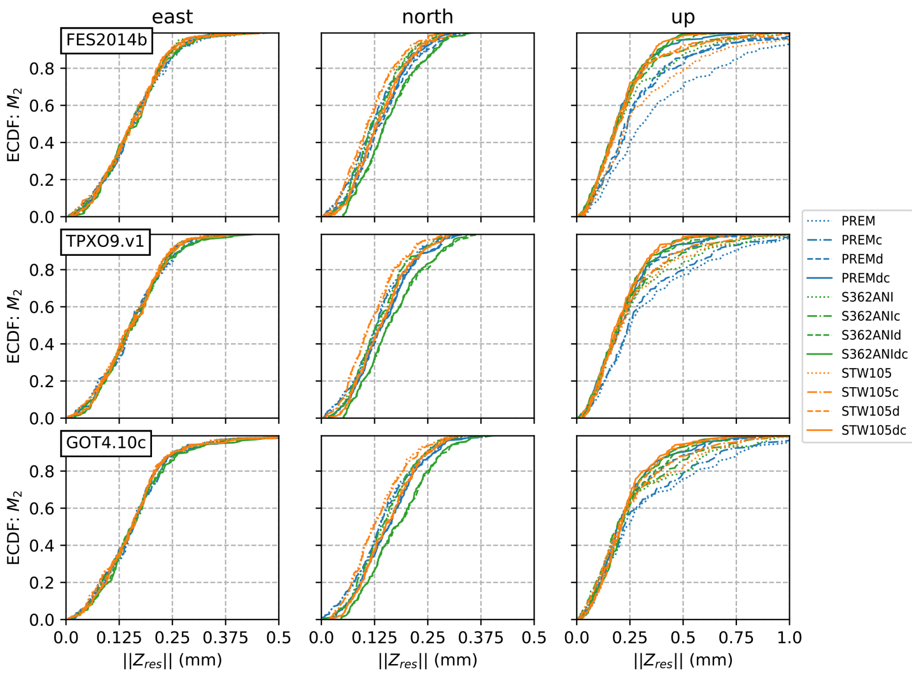

Figure S7.2. Same as Figure S7.1 but with mean residual OTL vector removed for each set of modeled values for the east, north and up components.

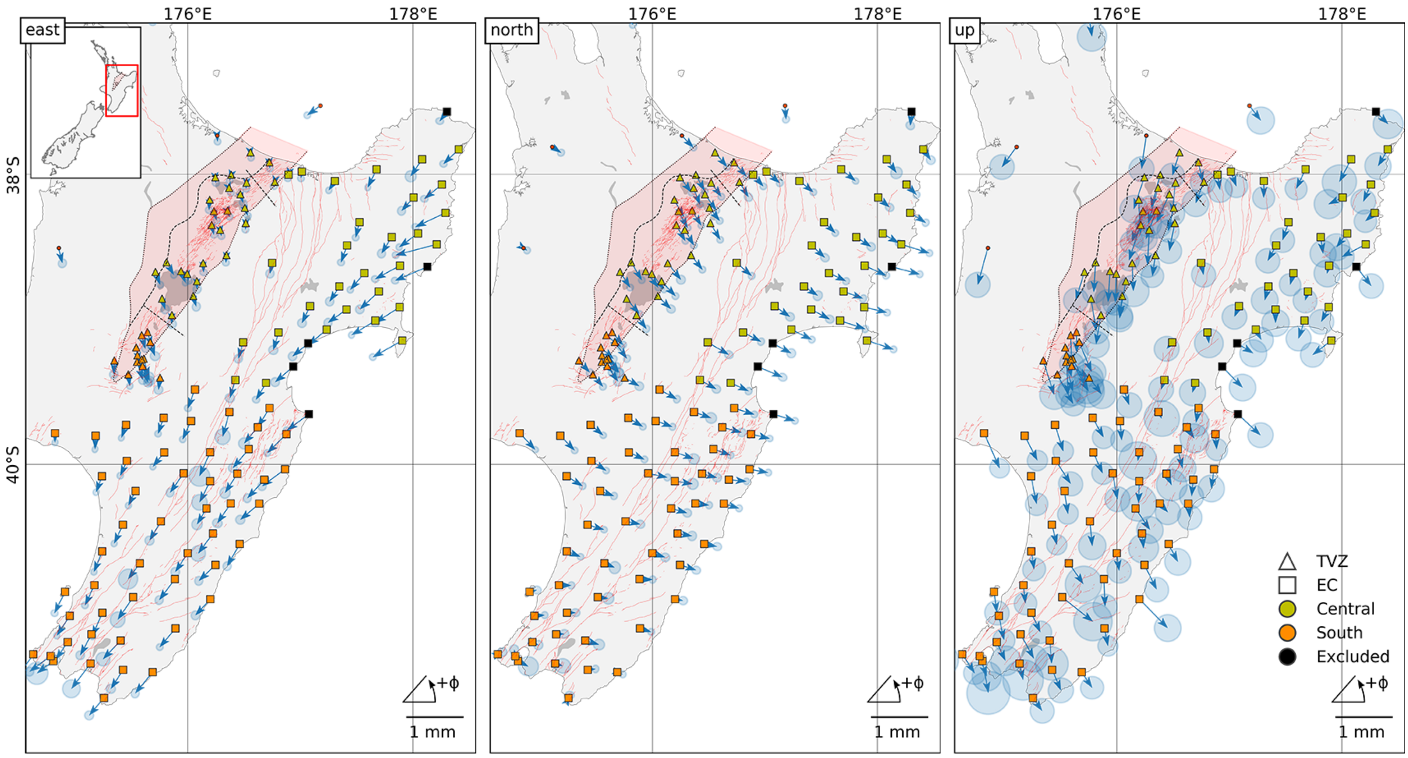

Figure S8. GPS-derived M_2 OTL residuals for a section of the North Island using FES2014b_STW105dc for east, north and up components. Sites are categorized into Taupo Volcanic Zone (TVZ) and East Coast (EC) regions (symbol shape) with subdivision of each into central and south along the TVZ central/south boundary (symbol color).

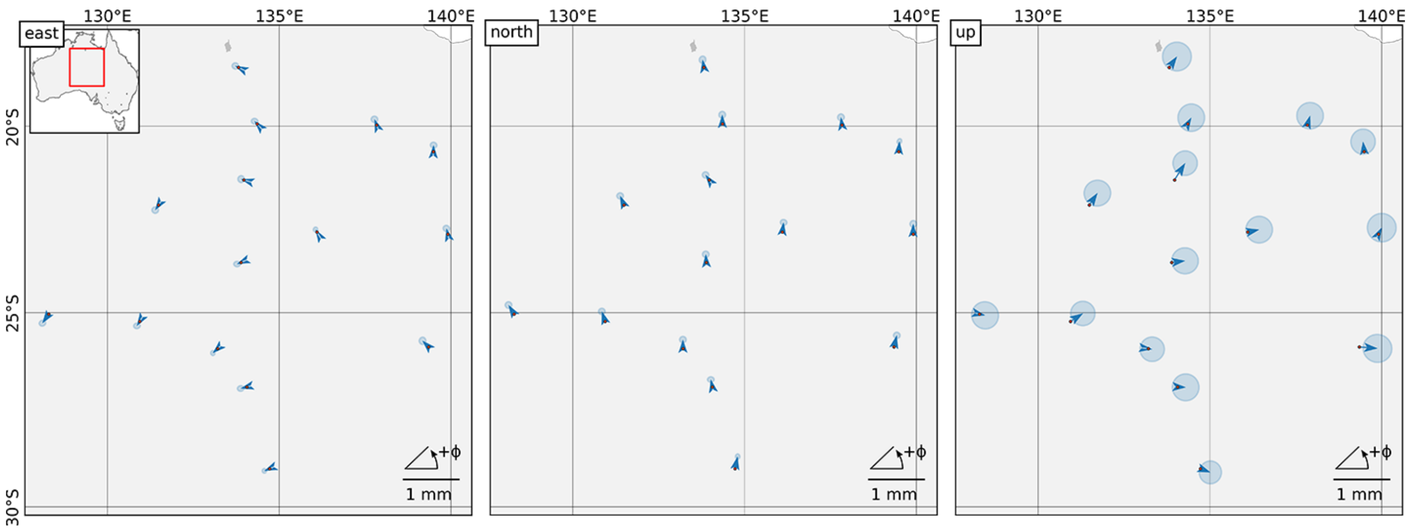

Figure S9. Residual OTL, $\|Z_{res}\|$, relative to FES2014b ocean tide model and STW105d Green's function (maximum bias in New Zealand dataset) for the east, north and up components derived at 14 inland Australian sites.

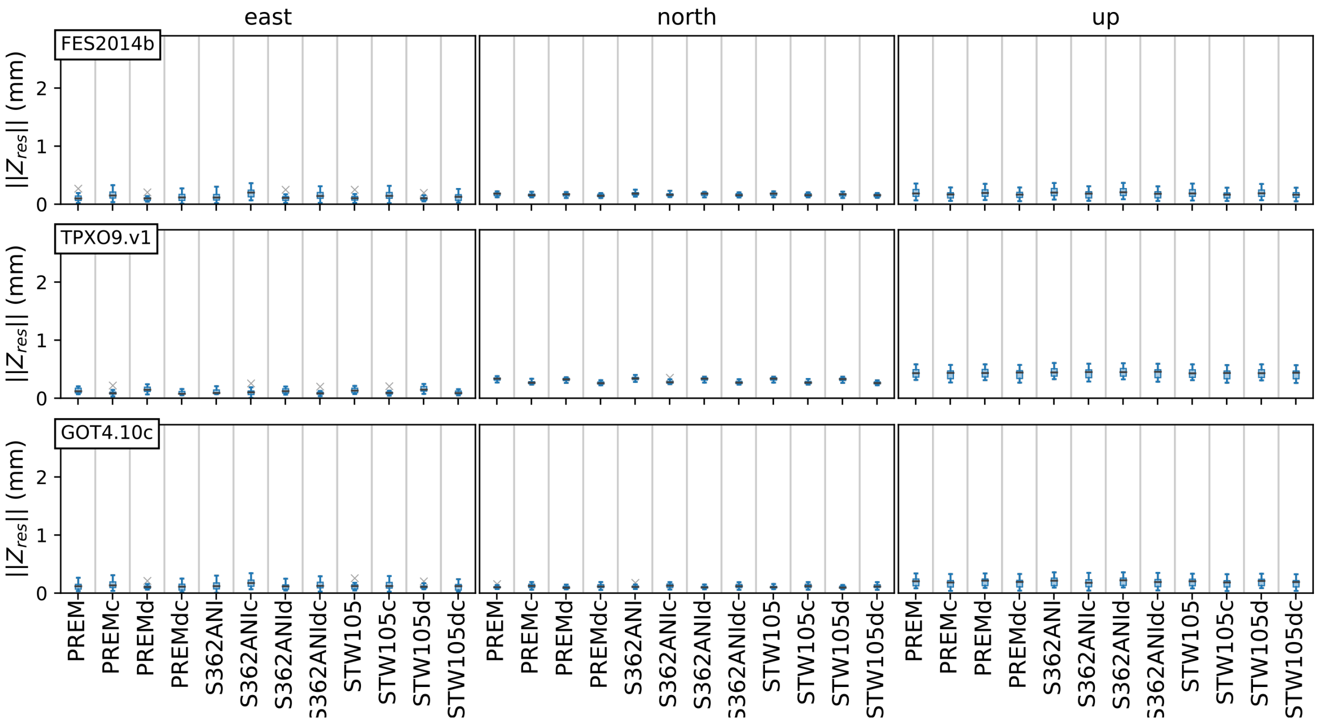

Figure S10. Residual OTL, $\|Z_{res}\|$, derived in the inland Australia relative to FES2014b, TPXO9.v1, GOT4.10c ocean tide models and a set of Green's functions for the east, north and up components.

Table S5. M_2 amplitude differences computed over 15 tide gauges relative to a set of ocean tide models. The bottom row shows an average amplitude difference per ocean tide model. The low value of FES2004 is associated with a low tide anomaly in the Hauraki Gulf. All values in meters.

TG	FES2004	FES2012	FES2014b	GOT4.10c	TPXO9	EEZ
AUCT	0.3371	1.0155	1.0042	0.8271	1.1103	1.2265
CHST	1.1169	1.0863	1.1056	1.1116	1.0897	1.1643
CPIT	0.6303	0.6275	0.6262	0.6199	0.6247	0.6642
GBIT	0.7730	0.7797	0.7895	0.8643	0.7698	0.8007
GIST	0.6313	0.6313	0.6316	0.6405	0.6305	0.6496
KAIT	0.6583	0.6423	0.6515	0.6405	0.6375	0.7078
LOTT	0.6947	0.7008	0.6946	0.7015	0.6933	0.7097
MNKT	1.1792	1.0872	1.0914	1.1545	1.0806	1.2510
NAPT	0.6694	0.6659	0.6595	0.6815	0.6476	0.7001
NCPT	0.7950	0.8070	0.7990	0.8021	0.7972	0.8150
OTAT	0.6939	0.7194	0.7179	0.7375	0.7590	0.7931
PUYT	0.7747	0.7782	0.7901	0.7604	0.7639	0.8394
SUMT	0.7838	0.8530	0.8481	0.8143	0.8235	0.9054
TAUT	0.7291	0.7177	0.7224	0.7225	0.7183	0.7566
WLGT	0.6251	0.3819	0.3809	0.3030	0.4199	0.5130
Avg. difference (m)	-0.0080	0.0295	0.0305	0.0113	0.0232	0.0841

Table S6. Q-values profiles* for PREM and STW105.

PREM

Depth (km)	Q
600.0	143.0
400.0	143.0
220.0	80.0
80.0	600.0
24.4	600.0
15.0	600.0

STW105

Depth (km)	Q
600.0	165.0
410.0	165.0
220.0	70.0
120.0	200.0
30.0	200.0
24.4	300.0
15.0	300.0

* from depth 220-80km PREM uses a Q of 80 and from a depth of 220-120km, STW105 uses a Q of 70. The last layer goes from a depth of 15km to the surface. No information is provided by the authors of either model on the uncertainty of Q values.

Table S7. Average residual amplitude (A) and phase (ϕ) values per each block. "c" and "s" indices stand for central and south blocks.

	TVZ_c		TVZ_s		EC_c		EC_s	
	A, mm	$\phi, ^\circ$	A, mm	$\phi, ^\circ$	A, mm	$\phi, ^\circ$	A, mm	$\phi, ^\circ$
east	0.15	-83.31	0.29	-78.61	0.37	-127.69	0.39	-122.87
north	0.32	-53.03	0.30	-43.96	0.33	-30.85	0.25	-8.62
up	0.51	-102.07	0.51	-70.29	0.26	-109.60	0.36	-71.66